First-principles phase diagram calculations for the rocksalt-structure quasibinary systems TiN–ZrN, TiN–HfN and ZrN–HfN

First-principles phase diagram calculations for the rocksalt-structure quasibinary systems TiN–ZrN, TiN–HfN and ZrN–HfN

Z T Y Liu[1], B P Burton[2], S V Khare[1] and D Gall[3]

[1] Department of Physics and Astronomy, University of Toledo, Toledo, OH 43606, USA
[2] Materials Measurement Laboratory, Metallurgy Division, National Institute of Standards and Technology (NIST), Gaithersburg, MD 20899, USA
[3] Department of Materials Science and Engineering, Rensselaer Polytechnic Institute, Troy, NY 12180, USA

E-mail: sanjay.khare@utoledo.edu

Abstract

We have studied the phase equilibria of three ceramic quasibinary systems $Ti_{1-x}Zr_xN$, $Ti_{1-x}Hf_xN$ and $Zr_{1-x}Hf_xN$ ($0 \leqslant x \leqslant 1$) with density functional theory, cluster expansion and Monte Carlo simulations. We predict consolute temperatures (T_C), at which miscibility gaps close, for $Ti_{1-x}Zr_xN$ to be 1400 K, for $Ti_{1-x}Hf_xN$ to be 700 K, and below 200 K for $Zr_{1-x}Hf_xN$. The asymmetry of the formation energy $\Delta E_f(x)$ is greater for $Ti_{1-x}Hf_xN$ than $Ti_{1-x}Zr_xN$, with less solubility on the smaller cation TiN-side, and similar asymmetries were predicted for the corresponding phase diagrams. We also analyzed different energetic contributions: ΔE_f of the random solid solutions were decomposed into a volume change term, ΔE_{vc}, and a chemical exchange and relaxation term, $\Delta E_{xc\text{-}rlx}$. These two energies partially cancel one another. We conclude that ΔE_{vc} influences the magnitude of T_C and $\Delta E_{xc\text{-}rlx}$ influences the asymmetry of $\Delta E_f(x)$ and phase boundaries. We also conclude that the absence of experimentally observed phase separation in $Ti_{1-x}Zr_xN$ and $Ti_{1-x}Hf_xN$ is due to slow kinetics at low temperatures. In addition, elastic constants and mechanical properties of the random solid solutions were studied with the special quasirandom solution approach. Monotonic trends, in the composition dependence, of shear-related mechanical properties, such as Vickers hardness between 18 to 23 GPa, were predicted. Trends for $Ti_{1-x}Zr_xN$ and $Ti_{1-x}Hf_xN$ exhibit down-bowing (convexity). It shows that mixing nitrides of same group transition metals does not lead to hardness increase from an electronic origin, but through solution hardening mechanism. The mixed thin films show consistency and stability with little phase separation, making them desirable coating choices.

S Online supplementary data available from stacks.iop.org/JPhysCM/29/035401/mmedia

(Some figures may appear in colour only in the online journal)

1. Introduction

Alloying has long been used to tune material properties. Studies of mixing typically focus on the stabilities of ordered intermediate ground state phases, end members, and the miscibility gaps between them. Some intermediate phases may be stable up to high temperatures, and may be optimal for certain applications. Disordered solid solutions may be desirable for applications that call for properties that are smoothly tuned by alloying.

A general theoretical goal has been the investigation of phase equilibria in ceramics. The key objective is to construct complete thermodynamic models to predict phase relations without resorting to experimental input. Such a first-principles approach has recently been developed. The cluster expansion (CE) formalism [1–6] fits the calculated formation energies of a small number of structures (~50–100) yielding a set of effective cluster interactions (ECIs) for pairs, triplets, quadruplets, etc. The energies to be fitted can be calculated with empirical potentials or first-principles approach such as density functional theory (DFT). This approach has been used to study a diverse set of material systems including alloys [7–14], semiconductors [15–18], ionic compounds [19–22], and minerals [23–26] with satisfactory results that compare favorably with experiments.

Rocksalt-structure early transition metal (TM) nitrides are known for their outstanding refractory properties such as high melting point, high hardness, high corrosion and oxidation resistance [27–31]. These nitrides, especially Group 4 TM nitrides, are relatively easy to fabricate with thin film deposition techniques, due to their large formation energies [32]. The simple structural prototype, rocksalt, turns out to be the most stable one of many other structures [32]. In contrast, late TM (platinum group metals) nitride formation has to rely on high-temperature and high-pressure conditions [33]. Adding to their individual superior properties, mixing them offers an additional promising route to more diverse material behaviors [34–46]. Here, we focus on using CE to study quasibinary mixing of nitrides of the Group 4 TMs, Ti, Zr and Hf; i.e. the systems $Ti_{1-x}Zr_xN$, $Ti_{1-x}Hf_xN$ and $Zr_{1-x}Hf_xN$ ($0 \leqslant x \leqslant 1$). Cation radii [47] for six-coordinated Ti^{4+}, Zr^{4+} and Hf^{4+} are 0.61 Å, 0.72 Å and 0.71 Å, respectively. These radii differences, Ti^{4+} from Zr^{4+}, and Ti^{4+} from Hf^{4+}, are large, and both the cations and anions are simple units, rather than groups like CO_3^{2-}. Hence, we anticipate simple mixing behavior and miscibility gaps. Phase separation is expected to happen when the solid solution is annealed below the consolute temperature (T_C). Such behavior was observed in $Ti_{1-x}Al_xN$ at 900–1000 °C [44, 48, 49]. However, experiments on $Ti_{1-x}Zr_xN$, including cathodic arc plasma deposited [50] and dc reactive magnetron sputtered [51] samples yielded single-phase materials after anealing at 600–1200 °C for hours; clearly, more experimental work would be appropriate. This discrepancy demands a better look at the driving force for decomposition, characterized by the difference of the undercooling annealing temperature from T_C. Previous estimates of T_C based on random solid solution mixing enthalpy and analytical entropy expressions, as high as 5000 K [50], call for more developed approaches that correctly consider configurational disorder and lattice vibrational free energy contributions at various temperatures. The CE formalism, coupled with subsequent Monte Carlo (MC) simulations, offers such an approach.

In this work, we study energy scales of the three systems and phase boundaries. We select the end members TiN, ZrN, HfN and ordered mixed structures to examine the electronic origin of instability. We analyze different contributions to random solid solution formation energies and explain the asymmetries of calculated miscibility gaps. For the nitride systems mentioned we set out to answer these questions: how the miscibility gaps appear and how they influence the decomposition process. In addition, we use the special quasirandom structure (SQS) approach [52–54] to independently model random solid solutions and compute their elastic constants. Comparison is made with results from the CE method and trends of mechanical properties are identified. We emphasize that although the SQS approach provides easy access to supercells that can be computed with DFT, it is designed only to model the high temperature, random solid solution configurations. In the SQS approach, entropy effects, under the ideal mixing assumption, and enthalpy corrections according to experiments need to be considered with analytical expressions to obtain approximate phase boundaries. On the other hand, the CE formalism is the only purely theoretical method to rigorously predict the full-temperature-range phase stability.

2. Computational methods

We performed *ab initio* DFT computations using the vienna *ab initio* simulation package (VASP) [55–58] with the projector-augmented wave method (PAW) [59, 60] and Purdew–Burke–Ernzerhoff (PBE) generalized gradient approximation (GGA) [61, 62]. We selected the potentials of Ti_sv, Zr_sv, Hf_pv and N, where '_sv' denotes that the semi-core s and p electrons are also included, while '_pv' specifies the semi-core p electrons. The plane wave energy cutoff was chosen to be 520 eV to ensure correct cell volume and shape relaxations. The *k*-point meshes were created with *k*-points per reciprocal atom (KPPRA) of 4000. Methfessel-Paxton order 1 smearing was used with a sigma value as small as 0.1 eV. The convergence criterion was set to 10^{-5} eV in energy during the electronic iterations. For structural optimization, the cell volume, shape and atomic positions were allowed to relax until stress was minimized and forces on any atom were below 0.02 eV Å^{-1}.

To obtain equations of state (EOS's) for TiN, ZrN and HfN, we picked 5 volume points in each case, fitted the total energies to the Birch–Murnaghan EOS [63], and derived the equilibrium volumes, energies and bulk moduli [32, 64].

Phase diagrams were generated for $Ti_{1-x}Zr_xN$, $Ti_{1-x}Hf_xN$ and $Zr_{1-x}Hf_xN$ using the alloy theoretic automated toolkit (ATAT) [65–68]. Included in ATAT, the MIT *Ab initio* Phase Stability (maps) [65, 66] code was used to generate the energy landscapes and CEs. The Easy Monte Carlo Code (emc2 and phb) [67, 68] was used to perform MC simulations to obtain the phase diagrams. With well-converged CEs, a box of $12 \times 12 \times 12$ 2-atom unit cells (1728 exchangeable sites) was chosen in the semi-grand canonical (SGC) ensemble simulations, in which chemical potential and temperature (T) can be given as external conditions. Chemical potential is defined as $\mu_i = \left(\frac{\partial G}{\partial n_i} \right)_{T, n_{j \neq i}}$, where G is the Gibbs free energy, n_i is the number of atoms of species i in the simulation cell. In

a binary system $A_{1-x}B_x$, $\mu = \mu_A - \mu_B$ is used as the input. For each μ and T point, sufficient MC passes were used to make sure the composition (x) reached a precision of 0.01. In a SGC ensemble the composition jumps from one boundary to another, skipping the two-phase region in response to the change in μ. This jumping prevents the determination of spinodal curves in this ensemble.

Vibrational free energy contributions to the phase diagram were added through the stiffness versus length transferable force constants method (fitsvsl and svsl code in ATAT) [66, 69, 70]. It is based on the observation that bond length is typically a good predictor of bond stiffness for a given structure and given type of bonds. This approach has an advantage over the direct calculation of phonon contribution of all structures in a set because only a few structures are needed to derive the stiffness versus length relationship. Then this relationship is used to get the (a) force constants, (b) dynamical matrices, (c) phonon spectra and (d) vibrational free energies for all structures in the CE set. Quasiharmonic approximation considering volume expansion was used. In our calculations, we selected 6 structures to extract the information on the force constants. The minimum distance between displaced atoms was set to 9 Å, displacement of the perturbed atom to 0.2 Å, strain of the maximum volume sampled 0.01 with 3 volume sampling points, and a linear fit was performed.

To independently obtain the physical properties of the random solid solution configurations, we employed SQS's at three different compositions $x = 0.25$, 0.5 and 0.75 for each system. These structures can be readily obtained from the sqs2tdb code in ATAT. Each SQS contains 32 atoms (16 formula units, or 16 exchangeable sites).

We then used these SQS's to compute the elastic constants. The routine implements the stress–strain linear relation, and is implemented in our open-source Python package pyvaspworkflow [71], leveraging pymatgen [72]. Because finite cell models do not preserve the cubic symmetry of the random solid solution configurations, symmetrization needs to be performed on the 6×6 elastic matrix according to the symmetry operations of the rocksalt structure (space group $Fm\bar{3}m$, point group $m\bar{3}m$) to obtain only three independent elements C_{11}, C_{12} and C_{44} of the cubic crystal system. This was done using the pymatgen.analysis.elasticity package [72].

3. Results and discussion

3.1. Cell parameters of the end members

Table 1 shows the lattice parameters of TiN, ZrN and HfN. Volumes and total energies of the structures are given for the 2-atom formula unit. Experimental values are also listed [73–75]. Lattice parameters (a) and volumes compare well with experimental results with a small and consistent overestimation, while the bulk moduli (B) obtained from the EOS fitting show an underestimation. These deviations are due to the use of GGA in our DFT calculations and is a well-known consequence of this approximation [32, 33, 64, 76–79].

Table 1. Lattice paramters a, volumes per formula unit (V/f.u.), *ab initio* total energies per formula unit (E/f.u.) and bulk moduli (B) from EOS's of TiN, ZrN and HfN.

	a (Å)	V/f.u. (Å^3)	E/f.u. (eV)	B (GPa)
TiN	4.25	19.2	−19.63	259
	4.241[a]	19.1[a]		318[b]
ZrN	4.60	24.3	−20.38	240
	4.578[a]	24.0[a]		285[c]
HfN	4.54	23.4	−21.76	247
	4.525[a]	23.2[a]		276[c]

[a] Expt. from [73].
[b] Expt. from [74].
[c] Expt. from [75].

3.2. Formation energy landscapes and electronic structures

Figure 1 shows the formation energy landscapes, $\Delta E_f(x)$ of $Ti_{1-x}Zr_xN$, $Ti_{1-x}Hf_xN$ and $Zr_{1-x}Hf_xN$. Ground-state analyses were performed by using the CE to calculate ΔE_f for all symmetrically inequivalent structures with 16 or fewer cation sites. In addition, we evaluated ΔE_f of the structures corresponding to random solid solution configurations at different compositions and fitted them to a smooth curve.

The convex boundary of the energy landscape defined by the energies and compositions of structures calculated by DFT constitute the convex hull. In $Ti_{1-x}Zr_xN$ and $Ti_{1-x}Hf_xN$, all non-end-member structures have positive ΔE_f. The up-bowing (concavity) of the random solid solution curves reach 100 meV/f.u. for $Ti_{1-x}Zr_xN$ and 35 meV/f.u. for $Ti_{1-x}Hf_xN$, indicating miscibility gaps. There is little asymmetry of $\Delta E_f(x)$ in $Ti_{1-x}Zr_xN$ but much more in $Ti_{1-x}Hf_xN$, leaning to the smaller cation TiN-side. Such asymmetry should also result in asymmetry in the phase diagram of $Ti_{1-x}Hf_xN$. On the other hand, cation size mismatch in $Zr_{1-x}Hf_xN$ is small, leading to much smaller absolute values of ΔE_f (<20 meV/f.u.). Most $Zr_{1-x}Hf_xN$ structures have negative ΔE_f and there are more members on and close to the convex hull; hence ordering is predicted. Note that some CE enumerated structures (green crosses in figure 1) are slightly below the convex hull. These are spurious ground states that lie within the numerical errors of the fitting process for CE coefficients. In systems with many states near the convex hull, the miscibility gaps close at very low temperatures, as seen in section 3.3 for $Zr_{1-x}Hf_xN$. The random solid solution curve of $Zr_{1-x}Hf_xN$ exhibits down-bowing (convexity). This is in contrast to the up-bowing behavior seen in $Zr_{1-x}Hf_xC$ [80], although the energy scales are similar (10 meV/f.u.). It is likely due to the different electronegativities [81, 82] of C (2.55) and N (3.04), and that M–N ionic bonds are more spatially accommodating than M–C covalent bonds. Nevertheless, we anticipate low temperature disordering in this system, similar to $Zr_{1-x}Hf_xC$.

To discover the connection between the positive ΔE_f and the electronic structures, we selected three structures to draw the projected electronic density of states (DOS) in figure 2. This was done for each system, including the end member structures and one with $A_{0.5}B_{0.5}N$ bulk composition, where A and B are transition metals. The $A_{0.5}B_{0.5}N$ structure has
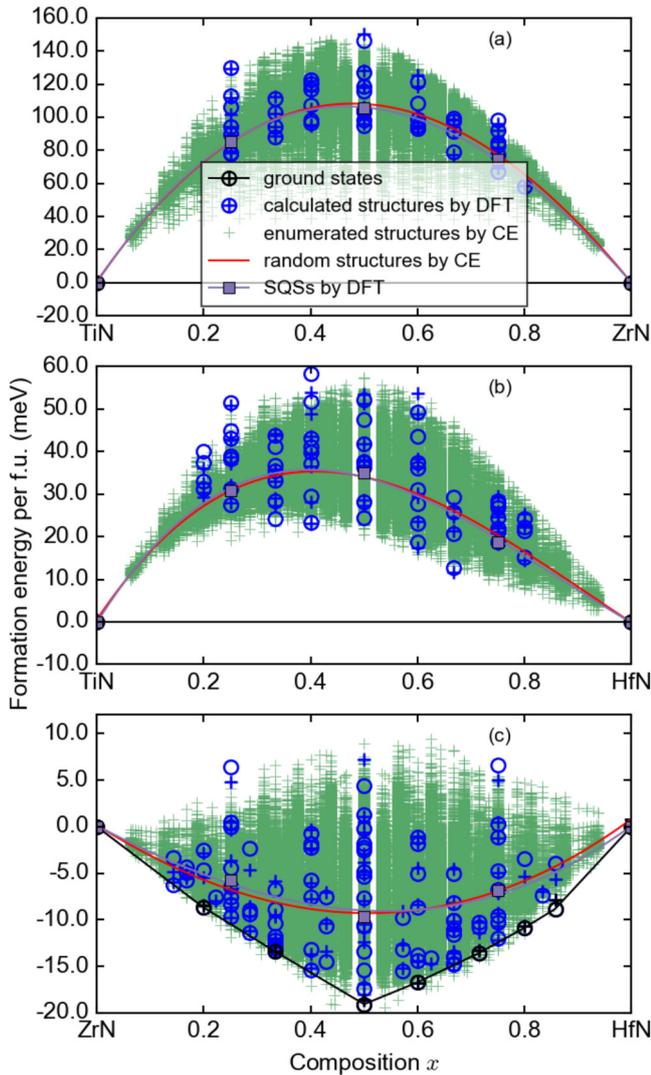
Figure 1. Formation energy landscapes of (a) $Ti_{1-x}Zr_xN$, (b) $Ti_{1-x}Hf_xN$ and (c) $Zr_{1-x}Hf_xN$. Energy values are per formula unit, i.e. per exchangeable site. Black markers and convex hull lines indicate ground states, blue markers indicate the structures calculated with DFT and used to obtain the CE, and green crosses indicate a 16-exchangeable-site ground-state analysis. Among the markers, hollow circles indicate DFT values, and crosses indicate CE-fitted values. Red curves indicate CE-fitted values of the random solid solution configurations, while purple squares and lines indicate DFT values and polynomial fit of the SQS's.

alternating A and B cations in the [1 1 1] direction. ΔE_f of this structure is positive in $Ti_{1-x}Zr_xN$ and $Ti_{1-x}Hf_xN$ and negative in $Zr_{1-x}Hf_xN$. In each of the three systems, the Fermi energy (E_F) is in the middle of a slope, indicating metallic behavior. Overlap between the transition metal d-states and nitrogen p-states, especially below E_F, indicates strong bonding. Comparing TiN, ZrN and HfN, Ti in TiN has a higher peak between 0–2 eV in the conduction band than Zr and Hf in their respective nitrides. This difference persists in their solid solutions $Ti_{0.5}Zr_{0.5}N$ and $Ti_{0.5}Hf_{0.5}N$, and could be another reason besides the cation size mismatch for their energetic disadvantage relative to the end members. In addition, we performed Crystal Orbital Hamilton Populations (COHP) [83] analyses to examine the bonding characteristics on these structures

and did not find noticeable indicators (figure S1 and table S1, supplemental material (stacks.iop.org/JPhysCM/29/035401/mmedia)).

Additionally, SQS's at different compositions were used to calculate ΔE_f for the random solutions, which are also depicted in figure 1. The fitted curves compare very well with the CE-fitted random solid solution curves in all three systems, validating the effectiveness of SQS in modeling random solid solution configurations. We reiterate that SQS needs to be combined with entropy contributions under ideal mixing assumption and experimental enthalpy corrections to obtain approximate phase boundaries. The CE formalism is capable of theoretically predicting the full-temperature-range phase stability with rigor.

3.3. Cluster expansions and phase diagrams

Table 2 summarizes the numbers of structures calculated with DFT, numbers of clusters, fitted ECIs and cross validation scores. Detailed information of the cluster sets and ECIs is provided in figure S2 and table S2 of the supplemental material.

Figure 3 shows the calculated phase diagrams of $Ti_{1-x}Zr_xN$, $Ti_{1-x}Hf_xN$ and $Zr_{1-x}Hf_xN$. Table 3 summarizes the resulting consolute temperatures (T_C). The first two systems feature simple miscibility gaps with T_C at 2400 K and 900 K, respectively. The asymmetry of the miscibility gap in $Ti_{1-x}Hf_xN$ is identified with the consolute point at $x_C \approx 0.3$. Similar asymmetry was also predicted for transition metal carbide systems $Ti_{1-x}Zr_xC$ and $Ti_{1-x}Hf_xC$ [80], and carbonate systems $Ca_{1-x}Mg_xCO_3$ and $Cd_{1-x}Mg_xCO_3$ [23, 25, 84]. There are multiple ground states in $Zr_{1-x}Hf_xN$, and phase transitions disappear above ~200 K. Computational time is unrealistically long to draw detailed boundaries of the many ground states. Therefore, we estimated their outer boundary through SGC ensemble simulations at different temperatures. We see abrupt changes in x with respect to μ in figure 3(d). When these abrupt changes disappear and the curves become smooth, the miscibility gaps are indicated to close up and the disordered solution phase is assumed to be stable. Based on this closure, we estimated the dotted curve in figure 3(c).

We included vibrational free energy contributions for $Ti_{1-x}Zr_xN$ and $Ti_{1-x}Hf_xN$, because there are miscibility gaps far above room temperature, and such contributions are likely to be significant. Figure S3 of the Supplemental Material illustrates the relationship between bond stiffness versus bond length and the linear fits. The Zr–N and Hf–N bonds behave similarly with large values, ~5 eV Å^{-2} for the stretching term at 2.24 Å, contrasting Ti-N, ~1 eV Å^{-2}, likely because of the difference in ionic radii. Vibrational contributions reduce T_C from 2400 K to 1400 K for $Ti_{1-x}Zr_xN$, and from 900 K to 700 K for $Ti_{1-x}Hf_xN$. The 42% drop in $Ti_{1-x}Zr_xN$ is large, but is also seen in ionic systems such as NaCl-KCl [19] and metallic systems such as Cr–Mo [7]. In comparison, Holleck [27, 85] estimated T_C to be 1850 K for $Ti_{1-x}Zr_xN$ and 1300 K for $Ti_{1-x}Hf_xN$, based on phenomenological thermodynamic models. Hoerling *et al* [50] estimated that for $Ti_{1-x}Zr_xN$ T_C was 5000 K based on regular solution mixing. No other
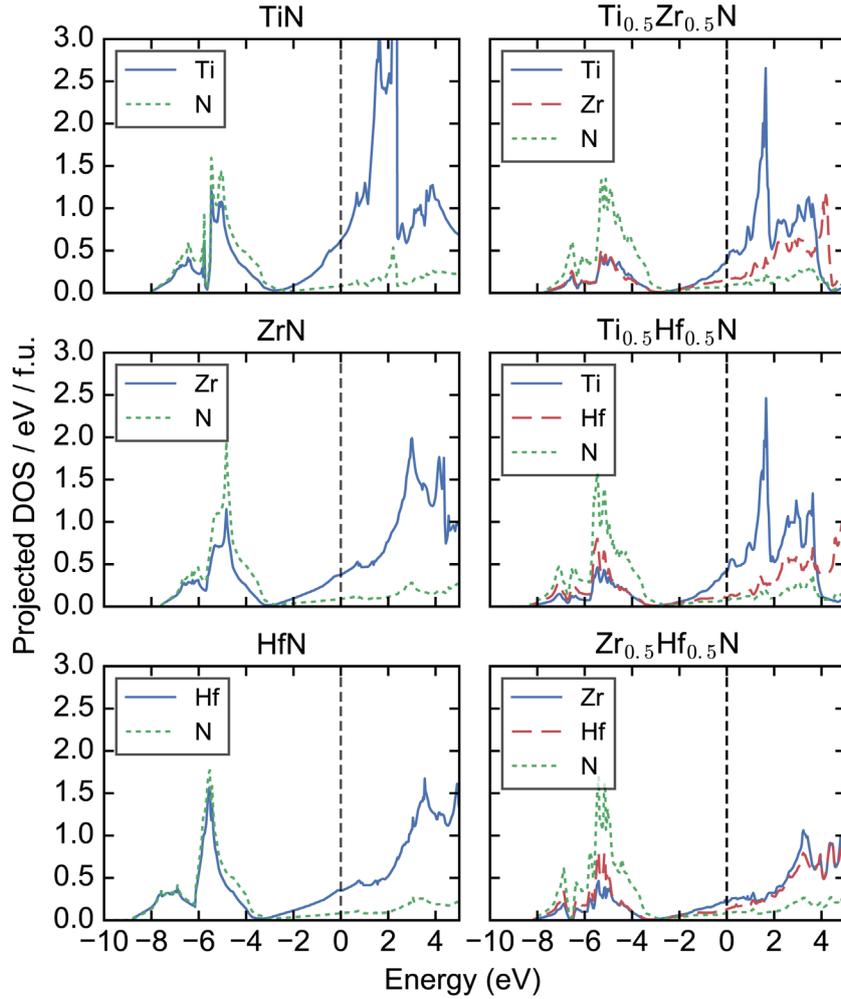
Figure 2. Projected density of states of TiN, ZrN, HfN and three solid solutions with composition $A_{0.5}B_{0.5}N$ where A and B are transition metals. The Fermi energy is set to 0.

Table 2. Numbers of structures calculated with DFT, numbers of clusters in pairs, triplets and quadruplets, and cross-validation (CV) score of $Ti_{1-x}Zr_xN$, $Ti_{1-x}Hf_xN$ and $Zr_{1-x}Hf_xN$.

	Num. of structures	Num. of clusters (pair + trip + quad)	CV score (meV)
$Ti_{1-x}Zr_xN$	45	15 + 7	5.2
$Ti_{1-x}Hf_xN$	74	16 + 7	3.8
$Zr_{1-x}Hf_xN$	95	32 + 23 + 3	2.6

estimates based on thermodynamic ensemble simulations, as in the present work, were found in the literature. However, experimental endeavors, including cathodic arc plasma deposited [50] and dc reactive magnetron sputtered [51] $Ti_{1-x}Zr_xN$ samples remained single-phase without decomposition after anealing at 600–1200 °C for hours. Only a slight broadening of an x-ray powder diffraction (XRD) peak was observed after a sample, with $x = 0.53$, was annealed at 1200 °C [50]. This observation is consistent with the initial stage of spinodal decomposition. Overall, experimental proof for phase separation in $Ti_{1-x}Zr_xN$ and $Ti_{1-x}Hf_xN$ is lacking. Therefore, comparison is made for the carbide system $Ti_{1-x}Zr_xC$ in figure S4 of the supplemental material; it shows that vibrational free

energy contributions reduce T_C from 3200 K to 2250 K, matching the experimental value precisely [86]. Comparable to the $Ti_{1-x}Zr_xN$, vibrational contributions have a large effect (28%) on T_C in this system. The calculations were done with PBE potentials, and such precise agreement may be coincidental but the high accuracy is as expected [19, 23, 68]. For this reason, we used PBE rather than LDA [32, 64, 87, 88] to perform all the calculations. The difference LDA potentials make is T_C ~500 K higher for $Ti_{1-x}Zr_xN$ (table 3).

To visually evaluate the degree and nature of the phase separation interface at different temperatures within the miscibility gap, and the extent of separation, we tracked the configurations of $Ti_{0.5}Zr_{0.5}N$ in a canonical ensemble MC simulation in figure 4. Composition x, instead of μ is fixed, as the simulaiton cell is annealed at varous temperatures, including 3000 K (far above the miscibility gap), 1500 K (just above the miscibility gap 1400 K), 1200 K, 900 K and 300 K (within the miscibility gap). From 3000 K to 1500 K the difference in configurational order is negligible, demonstrating complete disorder as soon as the miscibility gap is closed. As temperature is reduced, phase separation appears. At 300 K, it is clear that phase separation is complete with sharp interfaces between TiN and ZrN. Our simulation shows a layered configuration at lower
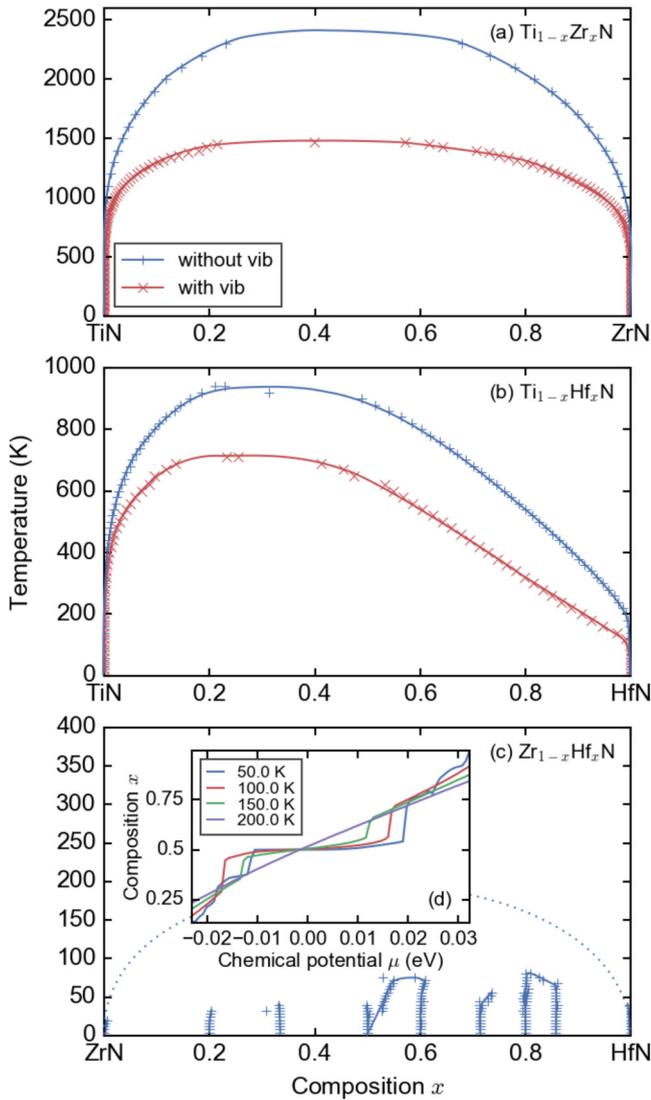
Figure 3. Calculated phase diagrams of (a) Ti$_{1-x}$Zr$_x$N, (b) Ti$_{1-x}$Hf$_x$N and (c) Zr$_{1-x}$Hf$_x$N. Small crosses are raw data points, and curves are interpolations and extrapolations. In (a) and (b), blue '+' and red '×' curves correspond to results without and with the vibrational contribution. In (c), the dotted curve indicates the estimated consolute boundary, as demonstrated by the inset (d). In (d), curves indicate compositions with respect to chemical potentials at various temperatures in a semi-grand-canonical ensemble. The abrupt changes disappear above 200 K, marking the consolute boundary.

temperatures. It is one of the many different outcomes from the Monte Carlo simulations. However, it does occur more often than segregated chunks. One explanation would be the system prefers to minimize the close interactions between Ti and Zr, and a planer separation leads to the smallest interface. In reality, the shapes of the phase aggregates are determined by separation mechanisms, such as nucleation and growth, or spinodal decomposition. The XRD peak-broadening observed by Hoerling *et al* [50], which would have been more prominent had the samples been annealed at ~900 °C and longer, is consistent with our simulation results.

Table 3. Consolute temperatures (T_C) of Ti$_{1-x}$Zr$_x$N, Ti$_{1-x}$Zr$_x$C, Ti$_{1-x}$Hf$_x$N and Zr$_{1-x}$Hf$_x$N. Vibrational free energy contributions are shortened as 'vib'.

	T_C without vib (K)	T_C with vib (K)	T_C from literature (K)
Ti$_{1-x}$Zr$_x$N	2400	1400	1850[a], 5000[b]
(with LDA)	2900	1800	
Ti$_{1-x}$Zr$_x$C	3200	2250	2250[c]
Ti$_{1-x}$Hf$_x$N	900	700	1300[a]
Zr$_{1-x}$Hf$_x$N	<200		

[a] From [27, 85].
[b] From [50].
[c] From [86].

3.4. Random solid solutions

Moler volume CEs were performed with the same cluster sets used for ΔE_f. Composition dependent volume deviations from linearity for random solid solutions are:

$$V_{linear} = (1 - x)V_{AN} + xV_{BN},$$

$$\text{Volume deviation of } A_{1-x}B_x N \equiv \frac{\left[V_{A_{1-x}B_xN} - V_{linear}\right]}{V_{linear}}. \quad (1)$$

Here A and B are Ti, Zr or Hf. Shown in figure 5, the random solid solutions of Ti$_{1-x}$Zr$_x$N and Ti$_{1-x}$Hf$_x$N have small positive deviations of about 1%. Positive deviations were also reported by Abadias *et al* [51], and in Ti$_{1-x}$Zr$_x$C and Ti$_{1-x}$Hf$_x$C [80]. On the other hand, negative deviations were predicted for various carbonate quasibinaries [84], likely due to the complex anion group CO_3^{2-}, which allows more geometric optimization than simple anions [89]. Calculated volume deviations in Zr$_{1-x}$Hf$_x$N are negligible, below 0.1%, because of the minimal cation size mismatch.

We separated solid solution mixing into two steps: (1) volume change (vc); and (2) chemical exchange and relaxation (xc-rlx), both relative to end members:

$$\Delta E_{vc}(A_{1-x}B_xN) = (1-x)\left[E_{AN}(V_{A_{1-x}B_xN}) - E_{AN}(V_{AN})\right]$$
$$+ x\left[E_{BN}(V_{A_{1-x}B_xN}) - E_{BN}(V_{BN})\right],$$
$$\Delta E_{xc\text{-}rlx}(A_{1-x}B_xN) = E(A_{1-x}B_xN) - (1-x)E_{AN}(V_{A_{1-x}B_xN})$$
$$- xE_{BN}(V_{A_{1-x}B_xN}),$$
$$\Delta E_f = \Delta E_{vc} + \Delta E_{xc\text{-}rlx}, \quad (2)$$

where $E_{AN}(V)$ and $E_{BN}(V)$ denote the EOS's of AN and BN. ΔE_{vc} describes the energy change due to the expansion or contraction of end member structures to the volume of the solid solution, and $\Delta E_{xc\text{-}rlx}$ measures the effect of the chemical exchange and solution cell shape and atomic position relaxation.

Figure 6 shows the ΔE_{vc} and $\Delta E_{xc\text{-}rlx}$ of the random solid solutions. In Ti$_{1-x}$Zr$_x$N and Ti$_{1-x}$Hf$_x$N, a large part of the ΔE_{vc} are canceled out by $\Delta E_{xc\text{-}rlx}$. In Zr$_{1-x}$Hf$_x$N the $\Delta E_{xc\text{-}rlx}$ is larger in absolute value than ΔE_{vc}. Comparing Ti$_{1-x}$Zr$_x$N and Ti$_{1-x}$Hf$_x$N, ΔE_{vc} of Ti$_{1-x}$Hf$_x$N is only ¾ of that of Ti$_{1-x}$Zr$_x$N, despite the almost identical cation radii of Ti and
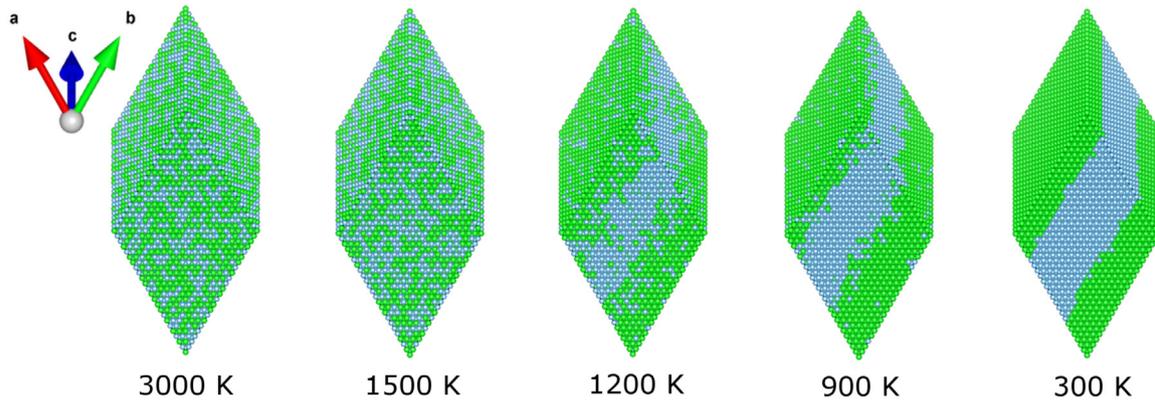
Figure 4. Monte Carlo simulation cells of $Ti_{0.5}Zr_{0.5}N$ at 3000 K (far above the miscibility gap), 1500 K (just above the miscibility gap 1400 K), 1200 K, 900 K and 300 K (within miscibility gap). Blue and green balls are Ti and Zr atoms. N atoms are omitted from the display for clarity. Increasing tendency towards separation is clearly visible with lowering temperature.
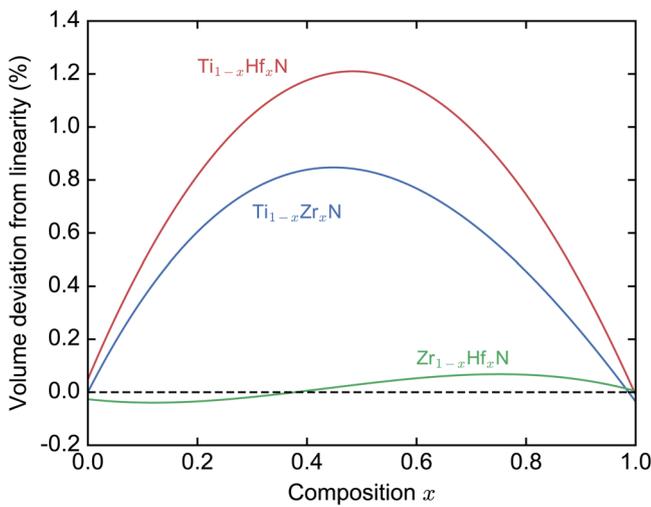
Figure 5. Volume deviations from linearity of $Ti_{1-x}Zr_xN$, $Ti_{1-x}Hf_xN$ and $Zr_{1-x}Hf_xN$. Curves indicate CE-fitted values of the random solid solution configurations.

Figure 6. Volume change and exchange-relaxation energies of $Ti_{1-x}Zr_xN$, $Ti_{1-x}Hf_xN$ and $Zr_{1-x}Hf_xN$. Values are per formula unit, i.e. per exchangeable site. Curves indicate CE-fitted values of the random solid solution configurations, with solid curves above the x-axis for the volume change energies (ΔE_{vc}), and dashed curves below for the exchange-relaxation energies ($\Delta E_{xc\text{-}rlx}$).

Zr. This is likely due to the combined effect of volume difference (ZrN 24.3 Å^3 versus HfN 23.4 Å^3) and bulk modulus difference (ZrN 240 GPa versus HfN 247 GPa). On the other hand, $\Delta E_{xc\text{-}rlx}$ of $Ti_{1-x}Zr_xN$ and $Ti_{1-x}Hf_xN$ are similar in magnitude. Therefore, ΔE_{vc} is the main reason for the difference in magnitude of ΔE_f in figures 1(a) and (b), and the consolute temperatures in figures 3(a) and (b), similarly in $Ti_{1-x}Zr_xC$ and $Ti_{1-x}Hf_xC$ [80].

In $Ti_{1-x}Zr_xN$ and $Ti_{1-x}Hf_xN$ the $\Delta E_{vc}(x)$ curves exhibit asymmetry, both with maxima on the smaller cation TiN-side. Similar results were calculated for carbide systems $Ti_{1-x}Zr_xC$ and $Ti_{1-x}Hf_xC$ [80], and nitride systems $Al_{1-x}In_xN$ and $Ga_{1-x}In_xN$ [16]. This asymmetry can be explained by the shape of end member EOS's, e.g. TiN in figure S5. It takes more energy to insert a larger ion into a smaller-volume crystal, than vice versa. The $\Delta E_{xc\text{-}rlx}(x)$ curve maximum for $Ti_{1-x}Hf_xN$ is less close to the TiN-side than $Ti_{1-x}Zr_xN$, resulting in more asymmetry of the final $\Delta E_f(x)$ curve for $Ti_{1-x}Hf_xN$ than $Ti_{1-x}Zr_xN$ in figure 1. These results were confirmed by SQS calculations. As stated in section 3.3, this asymmetry leads to the asymmetry in the calculated $Ti_{1-x}Hf_xN$ phase diagram in

figure 3(b). Surprisingly, asymmetry of the $Ti_{1-x}Hf_xC$ phase diagram is small [80]. We reproduced this phase diagram to confirm it. Thus, comparing $Ti_{1-x}Zr_xN$ and $Ti_{1-x}Hf_xN$ and $Ti_{1-x}Hf_xC$, strong or weak asymmetry of $\Delta E_f(x)$ and the resultant phase diagram can occure depending on the asymmetry of $\Delta E_{xc\text{-}rlx}(x)$, a quantity that measures the chemical exchange and cell shape and ionic relaxation. The mixing energy seperation illustrated above indicates that the size and shape of miscibility gaps are influenced by different processes.

3.5. Discussion on phase separation

Apparently, the experimental anealing temperature range 600–1200 °C is not sufficient undercooling, or atomic mobility is too low for $Ti_{1-x}Zr_xN$ to phase segregate [50]. This explanation is in agreement with the fact that phase separation was observed in $Ti_{1-x}Zr_xC$ but not in $Ti_{1-x}Zr_xN$. As listed in table 3, $Ti_{1-x}Zr_xC$ has a T_C of 2250 K while $Ti_{1-x}Zr_xN$ 1400 K.
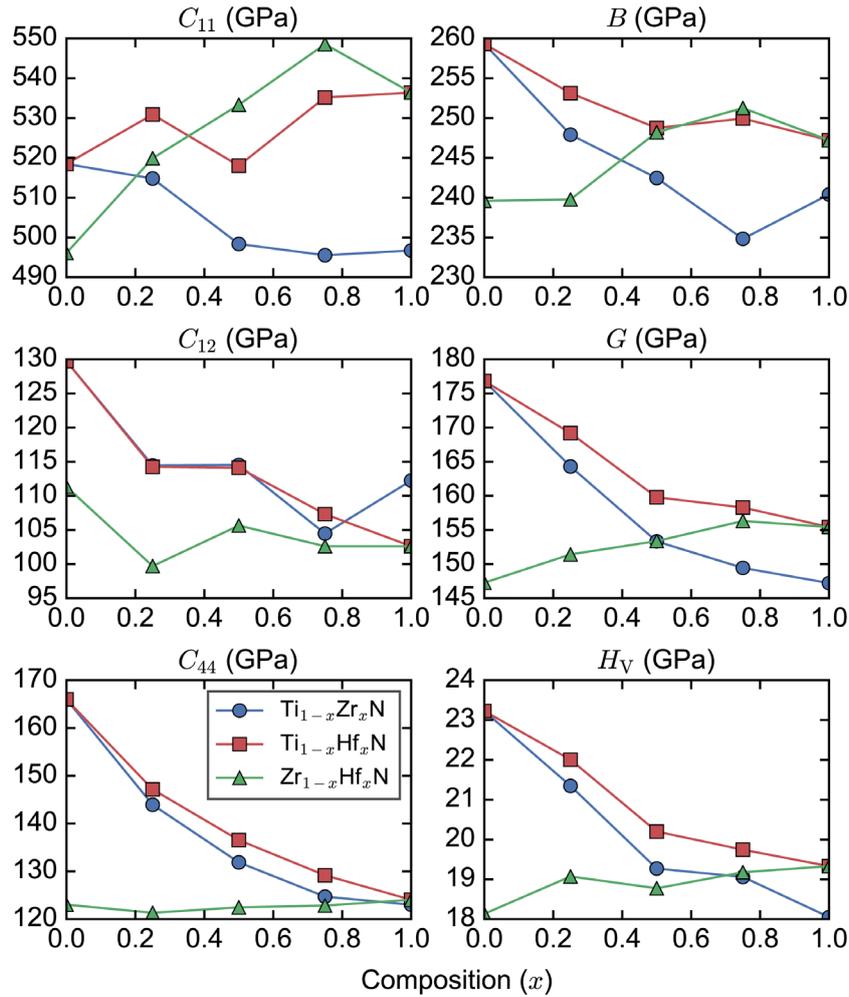
Figure 7. Elastic constants C$_{11}$, C$_{12}$, C$_{44}$, bulk moduli (B), shear moduli (G) and Vickers hardness (H_V) of the SQS's of Ti$_{1-x}$Zr$_x$N, Ti$_{1-x}$Hf$_x$N and Zr$_{1-x}$Hf$_x$N. Lines are a guide to the eye.

At the same temperature below both T_C, there is more under-cooling for Ti$_{1-x}$Zr$_x$C, therefore more driving force for phase separation. In addition, the bond dissociation energies for Ti–C (423 $\pm$ 30 kJ mol^{-1}) and Zr–C (495.8 $\pm$ 38.6 kJ mol^{-1}) are smaller than the corresponding Ti–N (476 $\pm$ 33 kJ mol^{-1}) and Zr–N (565 $\pm$ 25 kJ mol^{-1}) [90], so diffusion of TMs in nitrides is probably slower than in carbides. The above reasoning works similarly for Ti$_{1-x}$Hf$_x$N.

Moreover, it is noteworthy that the two systems Ti$_{1-x}$Zr$_x$N and Ti$_{1-x}$Hf$_x$N have no electronic incompatibility as is the case for Ti$_{1-x}$Al$_x$N [39, 91], because all three TMs belong to the same group. This results in the negative values of $\Delta E_{xc\text{-}rlx}$. For spinodal decomposition to be the preferential mechanism of phase separation, $\Delta E_{xc\text{-}rlx}$ needs to be positive, so that there is a chemical tendency for separation when volume change of emerging phases is inhibited, or slow in the initial stage. Therefore, nucleation and growth, where the energy advantage gained from volume change (positive ΔE_{vc}) counteracts the loss from chemical exchange (negative $\Delta E_{xc\text{-}rlx}$) to provide the driving force to get over the initial energy barrier is more likely to happen for systems like Ti$_{1-x}$Zr$_x$N and Ti$_{1-x}$Hf$_x$N. Such a chemical stability and solution hardening due to different cation radii make these two quasibinary systems ideal

for cutting tools applications within a typical temperature range of 600–900 °C.

3.6. Elastic and mechanical properties of the SQS's

Figure 7 shows the symmetrized elastic constants C$_{11}$, C$_{12}$ and C$_{44}$ and the derived mechanical properties, including bulk moduli (B), shear moduli (G), Pugh's ratios (k), Poisson's ratios (ν), and Vickers hardnesses (H_V) of the SQS's of Ti$_{1-x}$Zr$_x$N, Ti$_{1-x}$Hf$_x$N and Zr$_{1-x}$Hf$_x$N. All values are included in table S3 of the Supplemental Material. For detailed definitions and derivations see [32, 33, 64]. In particular we note that H_V was estimated with the formula $H_V = 0.92k^{1.137}G^{0.708}$, from Tian *et al* [92, 93] Among end members, TiN has the largest H_V, 23.2 GPa, followed by HfN with 19.3 GPa, and ZrN with 18.1 GPa. Although calculated trends for C$_{11}$ and C$_{12}$ are unclear, the shear-related quantities C$_{44}$, G and H_V in general exhibit monotonic behavior. The negative deviation from linearity in the calculations by Abadias *et al* [51] for Ti$_{1-x}$Zr$_x$N's shear modulus G is also seen here. This shows mixing nitrides of same group TMs does not lead to hardness increase from an electronic origin. Ramana *et al* [94] observed experimentally that with a higher concentration of

Zr in $Ti_{1-x}Zr_xN$, the hardness decreases, in agreement with our calculated trend. However, they also reported sensitive dependence of hardness on nitrogen flow percentage and substrate bias voltage in the DC reactive magnetron sputtering, ranging from 17 to 30 GPa. It was also observed that $Ti_{1-x}Zr_xN$ solid solutions can have hardness values reaching 40 Gpa [95], significantly higher than the two end members, likely due to solution hardening, where the cation size mismatch serves as dislocation impedence. It was also likely due to the Hall–Petch effect, which leads to enormous hardness increase with decreasing grain size, from ~20 GPa at 17 nm to ~40 GPa at 8 nm [96]. These plastic-deformation-related and microstructural aspects of hardness are not easily addressed in the first-principles framework.

4. Conclusions

We studied the phase equilibria of three ceramic quasibinary systems $Ti_{1-x}Zr_xN$, $Ti_{1-x}Hf_xN$ and $Zr_{1-x}Hf_xN$ $(0 \leqslant x \leqslant 1)$ with DFT, CE and MC simulations. Vibrational free energy contributions (vib) were also considered for $Ti_{1-x}Zr_xN$ and $Ti_{1-x}Hf_xN$. The consolute temperatures are 1400 K (2400 K without vib) for $Ti_{1-x}Zr_xN$, 700 K (900 K without vib) for $Ti_{1-x}Hf_xN$, and below 200 K for $Zr_{1-x}Hf_xN$ (without vib). The asymmetry of $\Delta E_f(x)$ is greater in $Ti_{1-x}Hf_xN$ than in $Ti_{1-x}Zr_xN$, with less solubility on the smaller cation TiN-side, and similar asymmetries were also predicted for the corresponding phase diagrams. ΔE_f of the random solid solutions were decomposed into a volume change (ΔE_{vc}) term and a chemical exchange and relaxation ($\Delta E_{xc\text{-}rlx}$) term. These two energies result in partial cancellation. We conclude that ΔE_{vc} influences the magnitude of consolute temperature while $\Delta E_{xc\text{-}rlx}$ influences the asymmetry of $\Delta E_f(x)$ and the phase boundaries. We also conclude that the absence of experimentally observed phase separation in $Ti_{1-x}Zr_xN$ and $Ti_{1-x}Hf_xN$ is probably due to a combined effect of insufficient undercooling, inadequate atomic diffusivity, and initial energy barrier for chemical exchange with constrained lattices.

In addition, elastic constants and mechanical properties of the random solid solutions were studied with the SQS approach. Monotonic trends, in the composition dependence, of shear-related mechanical properties, such as H_V between 18 to 23 GPa were predicted. Trends for $Ti_{1-x}Zr_xN$ and $Ti_{1-x}Hf_xN$ exhibit down-bowing behavior. It shows that mixing nitrides of same group TMs does not lead to hardness increase from an electronic origin, but through solution hardening mechanism. The mixed thin films show consistency and stability with little phase separation, making them desirable coating choices.

Acknowledgment

References

[1] Connolly J W D and Williams A R 1983 Density-functional theory applied to phase-transformations in transition-metal alloys *Phys. Rev.* B **27** 5169–72

[2] Sanchez J M, Ducastelle F and Gratias D 1984 Generalized cluster description of multicomponent systems *Physica* A **128** 334–50

[3] Ducastelle F 1991 *Order and Phase Stability in Alloys* (Amsterdam: Elsevier Science)

[4] De Fontaine D 1994 Cluster approach to order-disorder transformations in alloys *Solid State Phys.* **47** 33–176

[5] Zunger A 1994 *NATO ASI on Statics and Dynamics of Alloy Phase Transformation* vol 319, ed P E Turchi and A Gonis (New York: Plenum) p 361

[6] Laks D B, Ferreira L G, Froyen S and Zunger A 1992 Efficient cluster-expansion for substitutional systems *Phys. Rev.* B **46** 12587–605

[7] Chen W Z, Xu G L, Martin-Bragado I and Cui Y W 2015 Non-empirical phase equilibria in the Cr–Mo system: a combination of first-principles calculations, cluster expansion and Monte Carlo simulations *Solid State Sci.* **41** 19–24

[8] Liu J Z and Zunger A 2009 Thermodynamic theory of epitaxial alloys: first-principles mixed-basis cluster expansion of (In, Ga)N alloy film *J. Phys.: Condens. Matter* **21** 295402

[9] Ghosh G, van de Walle A and Asta M 2008 First-principles calculations of the structural and thermodynamic properties of bcc, fcc and hcp solid solutions in the Al–TM (TM = Ti, Zr and Hf) systems: a comparison of cluster expansion and supercell methods *Acta Mater.* **56** 3202–21

[10] Liu J Z, van de Walle A, Ghosh G and Asta M 2005 Structure, energetics, and mechanical stability of Fe–Cu bcc alloys from first-principles calculations *Phys. Rev.* B **72** 144109

[11] van de Walle A, Moser Z and Gasior W 2004 First-principles calculation of the Cu–Li phase diagram *Arch. Metall. Mater.* **49** 535–44

[12] Gao M C *et al* 2013 Phase stability and elastic properties of Cr–V alloys *J. Phys.: Condens. Matter* **25** 75402

[13] Barabash S V, Chepulskii R V, Blum V and Zunger A 2009 First-principles determination of low-temperature order and ground states of Fe–Ni, Fe–Pd, and Fe–Pt *Phys. Rev.* B **80** 220201

[14] Ravi C, Panigrahi B K, Valsakumar M C and van de Walle A 2012 First-principles calculation of phase equilibrium of V–Nb, V–Ta, and Nb–Ta alloys *Phys. Rev.* B **85** 54202

[15] Xue H T *et al* 2014 Phase equilibrium of a CuInSe2–CuInS2 pseudobinary system studied by combined first-principles calculations and cluster expansion Monte Carlo simulations *Mater. Sci. Semicond. Process.* **25** 251–7

[16] Burton B P, van de Walle A and Kattner U 2006 First principles phase diagram calculations for the wurtzite-structure systems AlN–GaN, GaN–InN, and AlN–InN *J. Appl. Phys.* **100** 113528

[17] Li X K, Xue H T, Tang F L and Lu W J 2015 First-principles calculation of sulfur-selenium segregation in $ZnSe_{1-x}S_x$: the role of lattice vibration *Mater. Sci. Semicond. Process.* **39** 96–102

[18] Burton B P, Demers S and van de Walle A 2011 First principles phase diagram calculations for the wurtzite-structure quasibinary systems SiC–AlN, SiC–GaN and SiC–InN *J. Appl. Phys.* **110** 23507

[19] Burton B P and van de Walle A 2006 First-principles phase diagram calculations for the system NaCl–KCl: the role of excess vibrational entropy *Chem. Geol.* **225** 222–9

[20] Burton B P and van de Walle A 2012 First principles phase diagram calculations for the octahedral-interstitial system αTiO_x, $0 \leqslant x \leqslant 1/2$ *CALPHAD* **39** 97–103

[21] Burton B P and van de Walle A 2012 First principles phase diagram calculations for the octahedral-interstitial system HfO_x, $0 \leqslant x \leqslant 1/2$ *CALPHAD* **37** 151–7

[22] Burton B P, van de Walle A and Stokes H T 2012 First principles phase diagram calculations for the octahedral-interstitial system ZrO_x, $0 \leqslant x \leqslant 1/2$ *J. Phys. Soc. Japan* **81** 14004

[23] Burton B P and van de Walle A 2003 First-principles-based calculations of the $CaCO_3$–$MgCO_3$ and $CdCO_3$–$MgCO_3$ subsolidus phase diagrams *Phys. Chem. Miner.* **30** 88–97

[24] Vinograd V L, Winkler B, Putnis A, Gale J D and Sluiter M H F 2006 Static lattice energy calculations of mixing and ordering enthalpy in binary carbonate solid solutions *Chem. Geol.* **225** 304–13

[25] Vinograd V L, Burton B P, Gale J D, Allan N L and Winkler B 2007 Activity-composition relations in the system $CaCO_3$–$MgCO_3$ predicted from static structure energy calculations and Monte Carlo simulations *Geochim. Cosmochim. Acta* **71** 974–83

[26] Vinograd V L, Sluiter M H F and Winkler B 2009 Subsolidus phase relations in the $CaCO_3$–$MgCO_3$ system predicted from the excess enthalpies of supercell structures with single and double defects *Phys. Rev.* B **79** 104201

[27] Holleck H 1986 Material selection for hard coatings *J. Vac. Sci. Technol.* A **4** 2661–9

[28] Sundgren J-E and Hentzell H T G 1986 A review of the present state of art in hard coatings grown from the vapor phase *J. Vac. Sci. Technol.* A **4** 2259

[29] Musil J 2000 Hard and superhard nanocomposite coatings *Surf. Coat. Technol.* **125** 322–30

[30] Georgson M, Roos A and Ribbing C-G 1991 The influence of preparation conditions on the optical properties of titanium nitride based solar control films *J. Vac. Sci. Technol.* A **9** 2191

[31] Niyomsoan S, Grant W, Olson D L and Mishra B 2002 Variation of color in titanium and zirconium nitride decorative thin films *Thin Solid Films* **415** 187–94

[32] Liu Z T Y, Zhou X, Khare S V and Gall D 2014 Structural, mechanical and electronic properties of 3d transition metal nitrides in cubic zincblende, rocksalt and cesium chloride structures: a first-principles investigation *J. Phys.: Condens. Matter* **26** 25404

[33] Liu Z T Y, Gall D and Khare S V 2014 Electronic and bonding analysis of hardness in pyrite-type transition-metal pernitrides *Phys. Rev.* B **90** 134102

[34] Tian F *et al* 2003 Epitaxial $Ti_{1-x}W_xN$ alloys grown on $MgO(0\,0\,1)$ by ultrahigh vacuum reactive magnetron sputtering: electronic properties and long-range cation ordering *J. Vac. Sci. Technol.* A **21** 140

[35] Alling B *et al* 2007 Mixing and decomposition thermodynamics of c-$Ti_{1-x}Al_xN$ from first-principles calculations *Phys. Rev.* B **75** 045123

[36] Alling B, Karimi A and Abrikosov I A 2008 Electronic origin of the isostructural decomposition in cubic $M_{1-x}Al_xN$ (M = Ti, Cr, Sc, Hf): a first-principles study *Surf. Coat. Technol.* **203** 883–6

[37] Gall D, Stoehr M and Greene J E 2001 Vibrational modes in epitaxial $TiScN(0\,0\,1)$ layers: an *ab initio* calculation and Raman spectroscopy study *Phys. Rev.* B **64** 174302

[38] Holec D, Rovere F, Mayrhofer P H and Barna P B 2010 Pressure-dependent stability of cubic and wurtzite phases within the TiN–AlN and CrN–AlN systems *Scr. Mater.* **62** 349–52

[39] Holec D *et al* 2011 Phase stability and alloy-related trends in Ti–Al–N, Zr–Al–N and Hf-Al-N systems from first principles *Surf. Coat. Technol.* **206** 1698–704

[40] Holec D, Zhou L, Rachbauer R and Mayrhofer P H 2013 Alloying-related trends from first principles: an application to the Ti–Al–X–N system *J. Appl. Phys.* **113** 113510

[41] Holec D *et al* 2014 Macroscopic elastic properties of textured ZrN–AlN polycrystalline aggregates: from *ab initio* calculations to grainscale interactions *Phys. Rev.* B **90** 184106

[42] Zhou L C, Holec D and Mayrhofer P H 2013 First-principles study of elastic properties of cubic $Cr_{1-x}Al_xN$ alloys *J. Appl. Phys.* **113** 043511

[43] Holec D, Franz R, Mayrhofer P H and Mitterer C 2010 Structure and stability of phases within the NbN–AlN system *J. Phys. D: Appl. Phys.* **43** 145403

[44] Mayrhofer P H *et al* 2003 Self-organized nanostructures in the Ti-Al-N system *Appl. Phys. Lett.* **83** 2049–51

[45] Deng R, Evans S R and Gall D 2013 Bandgap in $Al_{1-x}Sc_xN$ *Appl. Phys. Lett.* **102** 112103

[46] Leyendecker T, Lemmer O, Esser S and Ebberink J 1991 The development of the PVD coating TiAlN as a commercial coating for cutting tools *Surf. Coat. Technol.* **48** 175–8

[47] Shannon R D 1976 Revised effective ionic radii and systematic studies of interatomic distances in halides and chalcogenides *Acta Crystallogr.* A **32** 751–67

[48] Hörling A, Hultman L, Odén M, Sjölén J and Karlsson L 2005 Mechanical properties and machining performance of $Ti_{1-x}Al_xN$-coated cutting tools *Surf. Coat. Technol.* **191** 384–92

[49] Hörling A, Hultman L, Odén M, Sjölén J and Karlsson L 2002 Thermal stability of arc evaporated high aluminum-content $Ti_{1-x}Al_xN$ thin films *J. Vac. Sci. Technol.* A **20** 1815

[50] Hoerling A *et al* 2008 Thermal stability, microstructure and mechanical properties of $Ti_{1-x}Zr_xN$ thin films *Thin Solid Films* **516** 6421–31

[51] Abadias G, Ivashchenko V I, Belliard L and Djemia P 2012 Structure, phase stability and elastic properties in the $Ti_{1-x}Zr_xN$ thin-film system: experimental and computational studies *Acta Mater.* **60** 5601–14

[52] Zunger A, Wei S H, Ferreira L G and Bernard J E 1990 Special quasirandom structures *Phys. Rev. Lett.* **65** 353–6

[53] Wei S H, Ferreira L G, Bernard J E and Zunger A 1990 Electronic-properties of random alloys—special quasirandom structures *Phys. Rev.* B **42** 9622–49

[54] van de Walle A *et al* 2013 Efficient stochastic generation of special quasirandom structures *CALPHAD, Comput. Coupling Phase Diagr. Thermochem.* **42** 13–8

[55] Kresse G and Furthmuller J 1996 Efficiency of *ab initio* total energy calculations for metals and semiconductors using a plane-wave basis set *Comput. Mater. Sci.* **6** 15–50

[56] Kresse G and Furthmuller J 1996 Efficient iterative schemes for *ab initio* total-energy calculations using a plane-wave basis set *Phys. Rev.* B **54** 11169–86

[57] Kresse G and Hafner J 1994 *Ab initio* molecular-dynamics simulation of the liquid-metal–amorphous-semiconductor transition in germanium *Phys. Rev.* B **49** 14251–69

[58] Kresse G and Hafner J 1993 *Ab initio* molecular dynamics for liquid metals *Phys. Rev.* B **47** 558–61

[59] Blöchl P E 1994 Projector augmented-wave method *Phys. Rev.* B **50** 17953–79

[60] Kresse G and Joubert D 1999 From ultrasoft pseudopotentials to the projector augmented-wave method *Phys. Rev.* B **59** 1758–75

[61] Perdew J P *et al* 1993 Atoms, molecules, solids, and surfaces—applications of the generalized gradient approximation for exchange and correlation (vol 46, Pg 6671, 1992) *Phys. Rev.* B **48** 4978

[62] Perdew J P *et al* 1992 Atoms, molecules, solids, and surfaces: applications of the generalized gradient approximation for exchange and correlation *Phys. Rev.* B **46** 6671–87

[63] Birch F 1947 Finite elastic strain of cubic crystals *Phys. Rev.* **71** 809–24

[64] Liu Z T Y, Zhou X, Gall D and Khare S V 2014 First-principles investigation of the structural, mechanical and electronic properties of the NbO-structured 3d, 4d and 5d transition metal nitrides *Comput. Mater. Sci.* **84** 365–73

[65] van de Walle A, Asta M and Ceder G 2002 The alloy theoretic automated toolkit: a user guide *CALPHAD, Comput. Coupling Phase Diagr. Thermochem.* **26** 539–53

[66] van de Walle A 2009 Multicomponent multisublattice alloys, nonconfigurational entropy and other additions to the alloy theoretic automated toolkit *CALPHAD, Comput. Coupling Phase Diagr. Thermochem.* **33** 266–78

[67] van de Walle A and Asta M 2002 Self-driven lattice-model Monte Carlo simulations of alloy thermodynamic properties and phase diagrams *Model. Simul. Mater. Sci. Eng.* **10** 521–38

[68] van de Walle A and Ceder G 2002 Automating first-principles phase diagram calculations *J. Phase Equilib.* **23** 348–59

[69] van de Walle A and Ceder G 2002 The effect of lattice vibrations on substitutional alloy thermodynamics *Rev. Mod. Phys.* **74** 11–45

[70] van de Walle A 2013 Methods for first-principles alloy thermodynamics *JOM* **65** 1523–32

[71] Liu Z T Y 2016 pyvasp-workflow, a simple yet flexible programmatic workflow of describing, submitting and analyzing VASP jobs https://github.com/terencezl/pyvasp-workflow

[72] Ong S P *et al* 2013 Python materials genomics (pymatgen): a robust, open-source python library for materials analysis *Comput. Mater. Sci.* **68** 314–9

[73] Powder Diffraction Files: 03-065-0565 (TiN), 00-035-0753 (ZrN), 00-033-0592 (HfN), (International Center for Diffraction Data) PDF-2 www.icdd.com/products/pdf2.htm

[74] Kim J O, Achenbach J D, Mirkarimi P B, Shinn M and Barnett S A 1992 Elastic-constants of single-crystal transition-metal nitride films measured by line-focus acoustic microscopy *J. Appl. Phys.* **72** 1805–11

[75] Heid R, Bohnen K-P, Renker B, Wolf T and Schober H 2005 *Ab initio* lattice dynamics and electron-phonon coupling in the refractory compounds ZrN and HfN *Phys. Rev.* B **71** 92302

[76] Efthimiopoulos I *et al* 2015 Pressure-induced transition in the multiferroic CoCr$_2$O$_4$ spinel *Phys. Rev.* B **92** 64108

[77] Efthimiopoulos I *et al* 2016 Structural transition in the magnetoelectric ZnCr$_2$Se$_4$ spinel under pressure *Phys. Rev.* B **93** 174103

[78] Wang Y *et al* 2016 Thermal equation of state of silicon carbide *Appl. Phys. Lett.* **108** 61906

[79] Zhou X, Gall D and Khare S V 2014 Mechanical properties and electronic structure of anti-ReO$_3$ structured cubic nitrides, M3N, of d block transition metals M: an *ab initio* study *J. Alloys Compd.* **595** 80–6

[80] Adjaoud O, Steinle-Neumann G, Burton B P and van de Walle A 2009 First-principles phase diagram calculations for the HfC–TiC, ZrC–TiC, and HfC–ZrC solid solutions *Phys. Rev.* B **80** 134112

[81] Pauling L 1960 *The Nature of the Chemical Bond and the Structure of Molecules and Crystals: an Introduction to Modern Structural Chemistry* (Ithaca, NY: Cornell University Press)

[82] Allred A L 1961 Electronegativity values from thermochemical data *J. Inorg. Nucl. Chem.* **17** 215–21

[83] Dronskowski R and Blochl P E 1993 Crystal orbital hamilton populations (COHP)—energy-resolved visualization of chemical bonding in solids based on density-functional calculations *J. Phys. Chem.* **97** 8617–24

[84] Liu Z T Y, Burton B P, Khare S V and Sarin P 2016 First-principles phase diagram calculations for the carbonate quasibinary systems CaCO$_3$–ZnCO$_3$, CdCO$_3$–ZnCO$_3$, CaCO$_3$–CdCO$_3$ and MgCO$_3$–ZnCO$_3$ *Chem. Geol.* **443** 137–45

[85] Holleck H 1984 *Binary and Ternary Transition Metal Carbide and Nitride Systems (Binäre und ternäre Carbid- und Nitridsysteme der Übergangsmetalle)* (Stuttgart: Schweizerbart Science)

[86] Kieffer R and Ettmayer P 1970 Principles and latest developments in the field of metallic and nonmetallic hard materials *Angew. Chem., Int. Ed. Engl.* **9** 926–36

[87] Patil S K R, Mangale N S, Khare S V and Marsillac S 2008 Super hard cubic phases of period VI transition metal nitrides: first principles investigation *Thin Solid Films* **517** 824–7

[88] Patil S K R, Khare S V, Tuttle B R, Bording J K and Kodambaka S 2006 Mechanical stability of possible structures of PtN investigated using first-principles calculations *Phys. Rev.* B **73** 104118

[89] Chan J A and Zunger A 2009 II–VI oxides phase separate whereas the corresponding carbonates order: the stabilizing role of anionic groups *Phys. Rev.* B **80** 165201

[90] Haynes W M 2015 *CRC Handbook of Chemistry and Physics* 96th edn (Boca Raton, FL: CRC Press)

[91] Höglund C *et al* 2010 Effects of volume mismatch and electronic structure on the decomposition of ScAlN and TiAlN solid solutions *Phys. Rev.* B **81** 224101

[92] Chen X Q, Niu H Y, Li D Z and Li Y Y 2011 Modeling hardness of polycrystalline materials and bulk metallic glasses *Intermetallics* **19** 1275–81

[93] Tian Y J, Xu B and Zhao Z S 2012 Microscopic theory of hardness and design of novel superhard crystals *Int. J. Refract. Met. Hard Mater.* **33** 93–106

[94] Ramana J, Kumar S, David C and Raju V 2004 Structure, composition and microhardness of (Ti, Zr)N and (Ti, Al)N coatings prepared by DC magnetron sputtering *Mater. Lett.* **58** 2553–8

[95] Uglov V V *et al* 2004 Structural characterization and mechanical properties of Ti-Zr-N coatings, deposited by vacuum arc *Surf. Coat. Technol.* **180–1** 519–25

[96] Lin Y-W, Huang J-H and Yu G-P 2010 Effect of nitrogen flow rate on properties of nanostructured TiZrN thin films produced by radio frequency magnetron sputtering *Thin Solid Films* **518** 7308–11

[97] Ohio Supercomputer Center http://osc.edu/ark:/19495/f5s1ph73